


RESEARCH ARTICLE | MAY 23 2023

# Study on aerodynamic performance of inverted cone vertical axis wind turbine with different rotor configurations

Lei Zhang; Ao Wang; Jianjun Qu ; ... et. al



*Journal of Renewable and Sustainable Energy* 15, 033305 (2023)

<https://doi.org/10.1063/5.0145195>



CrossMark

## Articles You May Be Interested In

On the design and performance of a power electronics converter for the DeepWind project

*AIP Conference Proceedings* (July 2019)

A control algorithm for the deepwind floating vertical-axis wind turbine

*Journal of Renewable and Sustainable Energy* (December 2013)



**APL Energy**  
Bridging basic research and innovative technology that will impact the future

**First Articles Coming Soon!**  
No Article Processing Charges (APCs) through 2023



# Study on aerodynamic performance of inverted cone vertical axis wind turbine with different rotor configurations

Cite as: J. Renewable Sustainable Energy **15**, 033305 (2023); doi: [10.1063/5.0145195](https://doi.org/10.1063/5.0145195)  
Submitted: 3 February 2023 · Accepted: 8 May 2023 ·  
Published Online: 23 May 2023



View Online



Export Citation



CrossMark

Lei Zhang,<sup>1</sup>  Ao Wang,<sup>1</sup> Jianjun Qu,<sup>1,a)</sup>  and Ernesto Benini<sup>2</sup> 

## AFFILIATIONS

<sup>1</sup>School of Mechatronic Engineering, Harbin Institute of Technology, 150001 Harbin, China

<sup>2</sup>Department of Industrial Engineering, University of Padua, Via Venezia 1, 35131 Padua, Italy

<sup>a)</sup> Author to whom correspondence should be addressed: [qujianjun@hit.edu.cn](mailto:qujianjun@hit.edu.cn)

## ABSTRACT

Offshore wind resources are abundant. Vertical axis wind turbines (VAWTs) are suitable for working in the sea environment because of their low cost and high reliability. In this paper, an offshore floating inverted cone vertical axis wind turbine (ICVAWT) is proposed. The 3D unsteady computational fluid dynamics (CFD) method is utilized to model the ICVAWT. The turbulence model  $SST k - \omega$  is used to solve the Navier–Stokes equation, and the setting parameters of the solver and the independent grid are determined. The scale experimental prototype is designed using the similarity theory and the wind tunnel experiment is carried out. The experimental results verify the validity of the CFD model. The aerodynamic performance of nine ICVAWT configurations is analyzed by using the CFD model, and the effects of inverted cone angle and blade number on the power coefficient and operation stability of the ICVAWT are studied. It is found that when the inverted cone angle is  $45^\circ$ , and the number of blades is three (called the optimal configuration), the power coefficient is the highest at 0.309 (the optimal tip speed ratio is 3.5). With the increase in inverted cone angle and blade number, the fluctuation of wind turbine operating torque decreases. According to the distribution of each physical quantity in the flow field, the changes in aerodynamic performance are explained. Further research on the optimized configuration is carried out.

Published under an exclusive license by AIP Publishing. <https://doi.org/10.1063/5.0145195>

## I. INTRODUCTION

With the development of modernization, the demand for energy is getting higher and higher. However, the shortage of fossil energy and the resulting environmental problems are becoming increasingly serious. In responding to the requirements of climate change and energy demand, promoting energy transformation has become an important topic facing the whole world.<sup>1</sup> As a mature clean energy, wind energy is ideal energy for sustainable development. Large-scale development and utilization of wind energy have become an important way for countries to adjust their energy structure and achieve energy conservation and emission reduction goals.<sup>2,3</sup> The offshore wind resources are abundant, the annual average wind speed is higher than that on land, the turbulence intensity is low, and the wind shear effect is not obvious. It is very suitable to develop and utilize offshore wind energy, so it has attracted extensive attention from companies and research institutions in various countries.<sup>4</sup> The Global Wind Energy Report 2022 released by the GWEC showed that in 2021, the newly increased installation capacity of offshore wind reached

21.1 GW, creating a record for newly increased installation capacity of offshore wind and the total installed capacity of global offshore wind has reached 57 GW. The development potential of offshore wind energy is huge.<sup>5</sup>

The wind turbine is the main equipment that transforms wind energy into electrical energy. Based on the relationship between the rotation axis of the rotor and the wind speed direction, wind turbines can be classified into horizontal axis wind turbines (HAWTs) and vertical axis wind turbines (VAWTs). Nowadays, HAWTs have the largest number of installations and the widest range of applications in the world and occupy a dominant position in the wind market. VAWTs have good adaptability to different wind directions and can be installed on offshore planes. Compared with HAWTs, they have a low center of gravity and high reliability, which can greatly reduce the cost of installation, operation and maintenance. Therefore, they have great cost advantages. Many companies and research institutions have conducted research on offshore floating VAWTs.<sup>6–9</sup> The DeepWind project is a 5 MW offshore floating VAWT led by Risø DTU in

collaboration with 12 other universities, research institutions and industry, funded by the European FP7 program, aiming to cut down the development cost of deep-sea wind energy. DeepWind turbine consists of a two-blade Darrieus rotor and a floating platform fixed on the seabed by mooring, as shown in Fig. 1(a).<sup>10,11</sup> The European FP7 program also funded VertiWind 2 MW floating vertical axis wind turbine project. VertiWind VAWT consists of three groups of inclined blades, which can reduce blade stress and improve startup performance. The VAWT is fixed on the semi-submersible platform, as shown in Fig. 1(b).<sup>12</sup> MODEC Inc. of Japan has proposed a hybrid floating VAWT. The overwater part is a straight blade Darrieus VAWT placed on a floating platform, and the underwater part is a double-layer Savonius vertical axis wind turbine, which can provide starting torque and utilize water flow energy. The rated power of this VAWT is 50 kW, as shown in Fig. 1(c).<sup>13,14</sup> Sweden's company, SeaTwirl, has launched a 1 MW offshore floating VAWT. It uses straight blade VAWTs, which can work in sea areas with a water depth of 100 m and below and in extreme environments, and has advantages of high reliability and low cost as shown in Fig. 1(d).<sup>15</sup>

The offshore floating VAWTs have great advantages in utilizing offshore wind energy. The current floating VAWTs, including the prototypes, require long connecting arms and spindles, which brings difficulties for installing and maintaining and it is difficult to control the aerodynamic performance by variable pitch. At the same time, the alternating stress acting on the structure produces fatigue and reduces reliability. Qu *et al.*<sup>16</sup> proposed an innovative offshore floating VAWT, which removes the connecting arms and the main shaft. The blades are directly connected to the hub and the hub is equipped with a variable pitch mechanism which can independently control each blade. The center of gravity of the wind turbine is very low, which is suitable for installation and work at sea level. It can be transported to the offshore wind farm after installation at the shore, which improves its reliability. The purpose of this wind turbine is to reduce cost and obtain a high power coefficient. Because the blades of this VAWT rotate to form an inverted cone, this wind turbine is called an inverted cone vertical axis wind turbine (ICVAWT).

At present, the research on the aerodynamic performance of VAWTs mainly includes the analytical model method, computational fluid dynamics (CFD) method and wind tunnel experiment method.

Among them, the CFD method can simulate the running process of a wind turbine, obtain the aerodynamic performance and flow field changes, and could be employed to study the aerodynamic performance of a new VAWT and optimize its structure configuration. Vita *et al.*<sup>11</sup> the optimized blade shape of the DeepWind 5 MW VAWT through the aerodynamic performance calculation code HAWC2, and obtained the power output and coefficient of the DeepWind of the two blades, with a maximum power coefficient of 0.41. Bedon *et al.*<sup>17</sup> calculated aerodynamic performance of the DeepWind through the blade element momentum theorem (BEM), studied the effects of blade numbers and blade airfoils on the aerodynamic performance of the DeepWind, and optimized the chord distribution in the blade length direction. Finally, the best structural configuration of the DeepWind was obtained, and the maximum power coefficient was increased to 0.45. Carrigan *et al.*<sup>18</sup> used the CFD method combined with the finite difference evolution algorithm to optimize the blade thickness and solidity of the VAWT, which improved the starting ability by 6%. Bourguet *et al.*<sup>19</sup> also adopted the CFD method to optimize the blade with multiple constraints, aiming at reducing the weight of the blade and improving the aerodynamic performance. The finally obtained blade airfoil is very close to NACA0025. Golloy and Honra<sup>20</sup> used the CFD method of  $SST k - \omega$  model to simulate the aerodynamic performance of the VAWT with front swept surface wings, and compared it with the experiment results. The outcome indicated that the maximum power coefficient increased by 7.2% when the tip speed ratio (TSR) was 2.6. Almohammadi *et al.*<sup>21</sup> discussed the effect of different mesh grids on the aerodynamic performance of the straight blade VAWTs by solving 2D Navier–Stokes equations ( $RNG$  and  $SST k - \epsilon$  models, respectively) using the CFD method, and obtained the power coefficient independent of mesh grids. Lam and Peng<sup>22</sup> studied the near-field and far-field wake of the two straight blades VAWT, respectively, through 2D and 3D CFD methods and compared them with the particle image velocimetry (PIV) experiment test results. The velocity recovered 75% in the far field at a distance of ten times the diameter. Wang *et al.*<sup>23</sup> simulated the aerodynamic performance of adaptive blade Darrieus VAWT using the CFD method, and studied the effects of blade numbers and solidity on the power coefficient. The results showed that the power coefficient of the VAWT with deformable three blades increased by 14.56% at the low solidity. Zhang and Qu<sup>24</sup> used

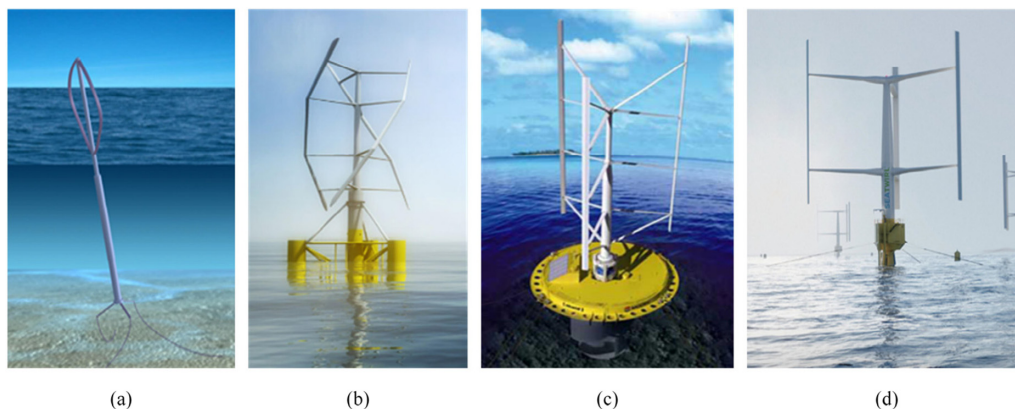


FIG. 1. Offshore floating VAWT concepts (a) DeepWind (b) VertiWind (c) SKWID (d) SeaTwirl.

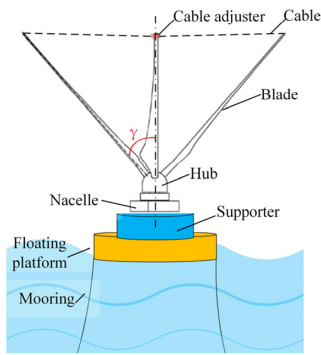


FIG. 2. Offshore floating ICVAWT geometry model.

the BEM method to carry out the theoretical model of a hybrid VAWT and compared it with CFD simulation results. The results were in good agreement. They studied the aerodynamic performance under different wind turbine structural parameters and found that the hybrid VAWT greatly improved the starting ability and had a high power coefficient. This paper will use the 3D unsteady CFD method to simulate the aerodynamic performance of ICVAWT. Meanwhile, it will study the effects of different wind turbine structural parameters on the aerodynamic performance, optimize the ICVAWT structural parameters, analyze the flow change law of the ICVAWT, and reveal the reasons affecting the aerodynamic performance of VAWT.

II. GEOMETRY MODEL

Figure 2 is the structural schematic diagram of offshore floating ICVAWT, which is composed of blades, hub, cables, cable adjuster, nacelle, support structure, floating platform and mooring system. The blades are directly connected to the hub. The included angle between the blade and the rotating shaft is defined as the inverted cone angle, which is expressed by  $\gamma$ . The top of each blade is connected to the cable adjuster with a cable to resist the blade deformation caused by centrifugal force and own weight. The rotor and the nacelle including the gearbox and generator are placed on the floating platform through the support structure, and the floating platform is fixed on the seabed through the mooring system. ICVAWT is suitable for working in the deep-sea environment.

This paper mainly studies the effects of the inverted cone angle and the number of the blades on the aerodynamic performance of ICVAWT. Therefore, the simple blade shape, constant cross section blade, is used to study the aerodynamic performance of ICVAWT in this paper as shown in Fig. 3. Symmetrical airfoil NACA0012 has been

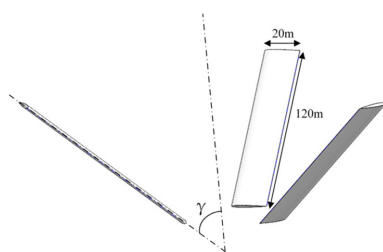


FIG. 3. Geometry model of the rotor.

TABLE I. The main parameters of the ICVAWT.

Description	Value	Unit
Rated power	2000	kW
Number of blades	2–4	
Blade chord length	20	m
Blade span	120	m
Blade airfoil	NACA 0012	
Angle	30–60	deg
Diameter of rotor	230	m
Cut in speed	5	m/s
Rated speed	10	m/s
Cut out speed	60	m/s

adopted, the blade chord is 20 m and the blade length is 120 m. The design-rated power of the offshore floating ICVAWT is 2 MW.

Table I describes the design parameters of the offshore floating ICVAWT.

III. CFD SIMULATION MODEL

A. Computational domain and mesh grid

ICVAWT has different sections at different heights, so 3D models have been used for numerical calculation. The size of the hub and cables relative to the blade is small, which has little impact on the aerodynamic performance of the ICVAWT. Therefore, the hub and cables were ignored in the geometric modeling, and only the blades were retained. Thus, the mesh quality would be improved, and the calculation speed would be accelerated, without affecting the result accuracy.

The computation domain of the ICVAWT is divided into two parts: the stationary domain and the rotating domain as shown in Fig. 4. The stationary domain size is  $6R \times 13R \times 26R$ , and the rotating domain is  $\phi 5R \times 2R$ .

The Stationary domain refers to the remote free incoming flow and the airflow change area after flowing through the VAWT. The stationary domain is obtained by subtracting the rotating domain from the whole computational domain. Taking the influence of the boundaries into consideration, the distance between the inlet of the stationary domain and the rotor center is 6.5 times the rotor radius, and the distance between the rotor center and the outlet is 19.5 times the rotor radius, which could well simulate the flow variation and the recovery process after flowing through the rotor. The diameter of the rotating domain is 2.5 times the diameter of the VAWT so that the flow around the rotor can be well simulated. The rotating domain is a

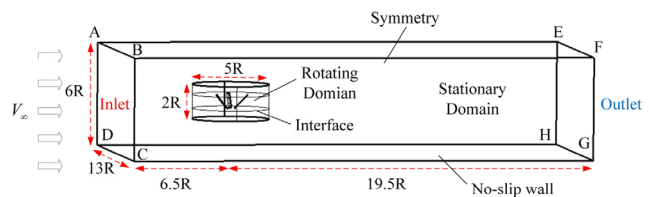


FIG. 4. Computation domain and boundary conditions of the rotor.



moving domain, including moving parts such as blades rotating with the rotating domain.

The airflow in the wind field belongs to subsonic incompressible flow, so the boundary conditions (Fig. 4) are adopted. For the inlet, the initial condition is the incoming flow velocity of 10 m/s, and the stationary domain boundary ABCD is set as the inlet boundary. The outlet pressure and velocity are unknown, so no initial condition needs to consider. Set the boundary surface EFGH as the pressure outlet boundary, and specify the atmospheric static pressure as 101.3 kPa. This computational domain is one of the same calculation domains in the real wind field, so the sides (face ADHE and face BCGF) are set as symmetry boundaries. The top (face ABFE) is set as symmetry boundary and the bottom (face CDHG) is set as no-slip wall boundary. Because the grids inside and outside the rotating domain need to be treated separately and the rotating domain rotates at a certain angular speed, the boundary of the cylindrical region containing the rotor is selected as the interface. The blades inside the rotating domain are set as the wall boundaries and rotate together with the rotating domain. The stationary domain and the rotating domain exchange data via the interfaces.

The software ICFM CFD was used to generate mesh grids in the computation domain. The unstructured mesh was used in the computational domains, and densification was carried out near the blades (Fig. 5), which can better reflect the airflow and force around the blades. Since the flow belongs to the low Reynolds number flow and flow detachment exists on the blades, the height of the first layer mesh of the blade is  $4 \times 10^{-5} \text{m}$ , the normal growth rate is 1.25 and the number of boundary layers is 15. After calculation,  $y^+$  value is 0.932 (less than 1). 833 715 elements are used on each blade and 3 123 517 elements are used in the computational domain.

### B. Turbulence model

The mass, momentum and energy transfer process in the fluid flow can be expressed by a set of differential equations and converted

into different forms. Then, the physical quantities of the flow field can be obtained by solving a group of algebraic equations and corresponding boundary conditions simultaneously.

The continuity equation of incompressible fluid is expressed in the following equation:

$$\frac{\partial}{\partial x_i}(\rho u_i) = 0. \tag{1}$$

The momentum Navier–Stokes equation is expressed in the following equation:

$$\frac{\partial}{\partial t}(\rho u_i) + \frac{\partial}{\partial x_j}(\rho u_i u_j) = -\frac{\partial P}{\partial x_i} + \rho f_i + \frac{\partial}{\partial x_j}(\bar{\tau}), \tag{2}$$

where  $P$  represents the static pressure,  $\rho f_i$  represents the gravity force and  $\bar{\tau}$  represents the stress tensor (described below). By assuming Stokes' hypothesis for Newtonian fluids, the stress tensor is given by the following equation:

$$\bar{\tau} = \mu \left[ \nabla \vec{v} + \nabla \vec{v}^T - \frac{2}{3} \nabla \vec{v} I \right], \tag{3}$$

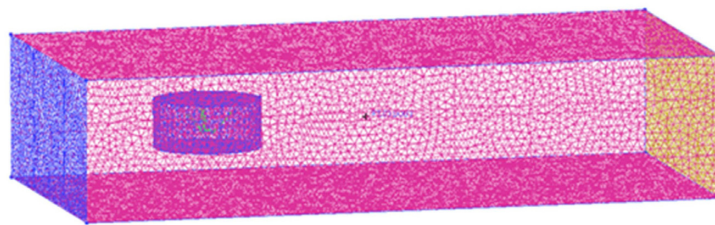
where  $\mu$  represents the dynamic viscosity.

Reynolds-averaged Navier–Stokes (RANS) equation is expressed in the following equation:

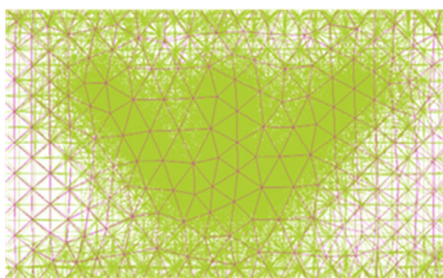
$$\frac{\partial}{\partial t}(\rho \bar{u}_i) + \frac{\partial}{\partial x_j}(\rho \bar{u}_i \bar{u}_j) = \rho \bar{f}_i - \frac{\partial \bar{p}}{\partial x_i} + \frac{\partial}{\partial x_j} \left( \mu \frac{\partial \bar{u}_i}{\partial x_j} - \rho \overline{u_i' u_j'} \right). \tag{4}$$

The flow around the rotor blades is incompressible, and there is a laminar-turbulent transition process. To simulate the fluid flow around the rotor in detail, the SST  $k-\omega$  turbulence model is selected.<sup>25,26</sup>

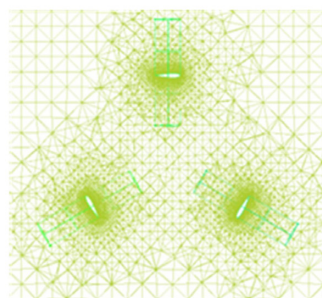
The turbulence kinetic energy  $k$  is obtained from the following transport equation:



(a)



(b)



(c)

FIG. 5. (a) Computational domain mesh (b) front view of the rotor mesh (c) top view of the rotor mesh and blade mesh.

$$\frac{\partial}{\partial t}(\rho k) + \frac{\partial}{\partial x_i}(\rho k u_i) = \frac{\partial}{\partial x_j} \left( \Gamma_k \frac{\partial k}{\partial x_j} \right) + G_k - Y_k + S_k + G_b. \quad (5)$$

The specific dissipation rate,  $\omega$ , is obtained from the following transport equation:

$$\frac{\partial}{\partial t}(\rho \omega) + \frac{\partial}{\partial x_i}(\rho \omega u_i) = \frac{\partial}{\partial x_j} \left( \Gamma_\omega \frac{\partial \omega}{\partial x_j} \right) + G_\omega - Y_\omega + S_\omega + G_{\omega b}. \quad (6)$$

The effective diffusivities for the SST  $k - \omega$  model are given by the following equations:

$$\Gamma_k = \mu + \frac{\mu_t}{\sigma_k}, \quad (7)$$

$$\Gamma_\omega = \mu + \frac{\mu_t}{\sigma_\omega}. \quad (8)$$

The turbulent viscosity is computed by combining  $k$  and  $\omega$  as follows:

$$\mu_t = \alpha^* \frac{\rho k}{\omega}. \quad (9)$$

### C. Solver settings

ANSYS Fluent 2021R1 software was used for the numerical calculation of ICVAWT. An unsteady implicit double precision pressure solver was used to solve the incompressible N-S equation. The solver adopted the separation type, the velocity and pressure coupling algorithm adopted SIMPLEC, the pressure interpolation adopted the second-order format, and the second-order upwind format was adopted for discretizing the momentum equation. The standard interpolation method was adopted for the grid surface pressure calculation and the transient time was discretized by the second-order discrete scheme. The rest of the discrete formats were all in second-order format. The aerodynamic performance of the ICVAWT was analyzed by the interface mesh technique.

The transient solver was adopted in the simulation. Every  $2^\circ$  rotation of the ICVAWT is set as a time step, and the time step is  $\Delta t = \frac{\pi}{90\omega}$ . When the residuals reach the convergence criterion  $10^{-6}$ , the converged state is considered to be reached at each step. The number of convergence steps for the converged-state calculation is set to 40. Ten cycles are picked for the study, and the variation with the whole moment coefficient of the ICVAWT is shown in Fig. 6. The oscillation of the moment coefficient has a high value in the first four cycles called a transient period. After four cycles, the moment coefficients show a periodic variation and the amplitude tends to converge, which is called the fully developed period. Thus, the tenth cycle is used to study the ICVAWT performance when analyzing the transient data.

### D. Mesh independence test

Refine the mesh grid to different degrees, input the same parameter settings, respectively, and observe the variation of the moment coefficient of the VAWT. When the moment coefficient does not change significantly quantitatively with the change of the grid level, the grid refinement level at this time is called the Grid Independent

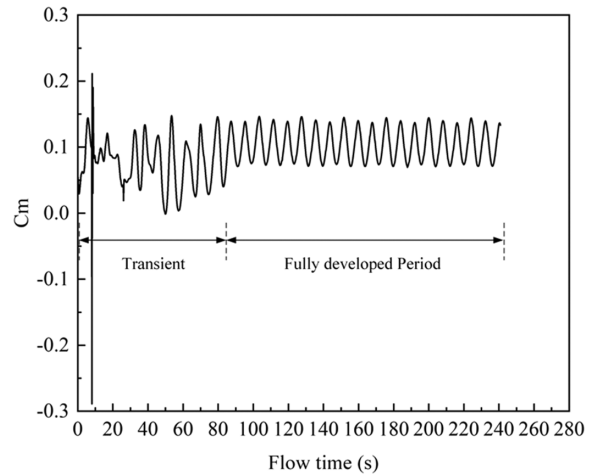


FIG. 6. Variation of moment coefficient for flow time, i.e., the period of rotation.

Limit (GIL). Using grid independent limit grid size for numerical calculation, on the one hand, can reduce the calculation amount of CPU and save the calculation time, on the other hand, can ensure the calculation accuracy and consistency. Table II shows the different refinement levels of the computational grids. The Variation of torque coefficient with number of elements was obtained by inputting the same parameters and solver settings for different numbers of elements, as shown in Fig. 7.

Figure 7 shows that with the number of elements increases, the moment coefficient of the ICVAWT shows an increasing trend. When the number of elements reaches  $3.12 \times 10^6$ , the torque coefficient basically does not change with the increase in the number of elements. Therefore, the mesh grid size with the number of elements of  $3.12 \times 10^6$  is the Grid Independence Limit of this case and this mesh grid size is adopted as the optimal grid for numerical calculation.

### E. Aerodynamic performance indicators

The aerodynamic performance of the ICVAWT was studied by changing the rotation speed of the ICVAWT. The rotation speed of the wind turbine can be expressed by the tip speed ratio (TSR), which

TABLE II. Details of refinement levels of the computation grids.

Refinement level	Number of nodes	Number of elements
1	1 860 569	873 460
2	2 347 669	1 382 799
3	2 479 057	1 741 764
4	3 301 025	2 181 088
5	3 791 457	2 500 136
6	4 322 954	2 850 612
7	4 735 240	3 122 479
8	6 833 553	3 950 125
9	7 753 674	4 806 871

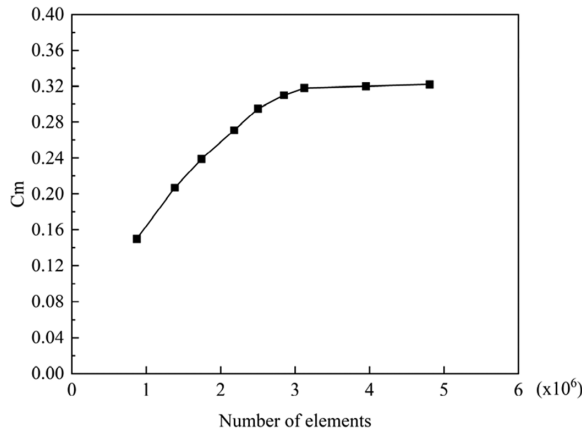


FIG. 7. Variation of torque coefficient with the number of elements of computational domain.

is defined as the ratio of the velocity of the blade tip of the VAWT to the free incoming wind velocity, expressed by the following equation:

$$\lambda = \frac{\omega R}{V_\infty}, \tag{10}$$

where  $R$  represents the maximum radius of the ICVAWT,  $\omega$  represents the angular speed and  $V_\infty$  represents the free incoming wind velocity.

The moment of the whole rotor is obtained by integrating the surface pressure of the blade grid in ANSYS Fluent. The moment coefficient  $C_M$  can be calculated by Eqs. (11) and (12). The performance of the ICVAWT is expressed by the power coefficient  $C_P$ , which is defined as the ratio of the energy obtained by the rotor and the energy carried by the free wind flow, that is, Eq. (13). The relationship between  $C_P$  and  $C_M$  is shown in Eq. (14)

$$C_M = \frac{M}{\frac{1}{2} \rho A V_\infty^2 R}, \tag{11}$$

$$C_M = \frac{1}{2\pi} \int_0^{2\pi} C_M(\theta) d\theta, \tag{12}$$

$$C_P = \frac{P}{\frac{1}{2} \rho A V_\infty^3} = \frac{M}{\frac{1}{2} \rho A V_\infty^2 R} \frac{\omega R}{V_\infty}, \tag{13}$$

$$C_P = \lambda \cdot C_M, \tag{14}$$

where  $R$  represents the maximum radius of the ICVAWT and  $A$  represents the swept area.

### F. Validation methodology of CFD numerical model

Wind tunnel experiments are used to verify the validity of the established CFD model. Using scale wind turbines to simulate actual full-scale wind turbines in the wind tunnel is a very effective way to study the aerodynamic performance of megawatt wind turbines through similarity theory. According to the similarity theory of fluid dynamics,<sup>27</sup> to ensure the similarity of the airflow process, it is

necessary to meet the geometric, motion and dynamic similarity. For ICVAWT, it can be expressed in the following equation:

$$\begin{aligned} \frac{L}{L_m} &= \frac{c_i}{c_{im}} = \frac{R_i}{R_{im}} = m_L, \\ \frac{V_\infty}{V_{\infty m}} &= \frac{V}{V_m} = \frac{\omega}{\omega_m} m_L = m_v, \\ \frac{dF_t}{dF_{tm}} &= \frac{dF_n}{dF_{nm}} = m_F, \end{aligned} \tag{15}$$

where  $L$  represents the blade length,  $c$  represents the blade chord,  $R_i$  represents the rotor radius,  $m_L$  represents the geometric similarity constant,  $V_\infty$  represents the free incoming wind velocity,  $v$  represents the blade velocity,  $\omega$  represents the rotating angular speed,  $m_v$  represents the velocity similarity constant,  $dF_t$  represents the tangential force,  $dF_n$  represents the normal force,  $m_F$  represents the force similarity constant.

Moment and power similarities are expressed in the following equation:

$$\begin{aligned} \frac{dM}{dM_m} &= \frac{R_i dF_t}{dF_{tm}} = \frac{\rho v^2}{\rho_m v_m^2} m_L^3, \\ \frac{dP}{dP_m} &= \frac{dM/dt}{dM_m/dt_m} = \frac{\rho v^3}{\rho_m v_m^3} m_L^2. \end{aligned} \tag{16}$$

Energy conversion efficiency of VAWT is expressed in the following equation:

$$C_p = \frac{M\omega}{P_{total}}, \tag{17}$$

where,  $P_{total}$  represents the power of the free incoming wind.

In combination with Eqs. (16) and (17), the similarity of power coefficient is obtained as follows:

$$\frac{C_p}{C_{pm}} = \frac{R\omega/V_\infty}{R_m\omega_m/V_{\infty m}} = \frac{\lambda}{\lambda_m}. \tag{18}$$

Equation (18) shows that the power coefficients of the two are the same when the TSR is equal. In this experiment, the geometric similarity constant  $m_L = 182$  is selected to ensure that the experimental machine and the full-scale machine operate at the same TSR. Table III shows the parameters of the experiment machine.

Figure 8 shows the designed scale wind turbine and components. The scale ICVAWT consists of blades, the dome, inverted cone angle adjusters, pitch motors, the collector ring, the transmission

TABLE III. The parameters of the experiment machine.

Description	Value	Unit
Rated power	65	W
Blade chord length	0.11	m
Blade span	0.66	m
Blade airfoil	NACA 0012	...
Rotor diameter	1.16	m
Wind tunnel speed	10	m/s

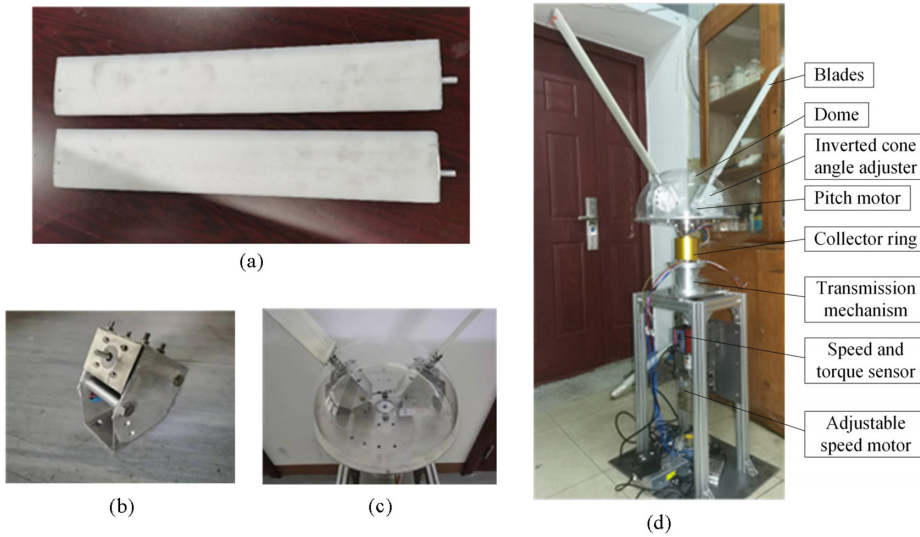


FIG. 8. Experiment machine and components (a) Blades (b) Inverted cone angle adjuster (c) The rotor (d) Experiment machine.

mechanism, the speed and torque sensor, the adjustable speed motor and so on.

Figure 9 shows the wind tunnel experiment principle and platform. The frequency converter controls the speed of the artificial wind source to generate different wind speeds. Uniform wind speed is formed at the outlet of the wind tunnel through the rectification. The dimension of the wind tunnel outlet is  $2.5 \times 2.5 \text{ m}^2$ . In this experiment, the wind speed at the outlet of the wind tunnel measured by the wind speed sensor is a uniform 10 m/s and the turbulence intensity is 3%. The center of the rotor and the outlet center of the wind tunnel is on the same horizontal line and the distance between the wind tunnel outlet and the experiment wind turbine is 1 m. The IPC is responsible for controlling the speed of the adjustable speed motor and collecting real-time data on the speed and torque sensor.

During the experiment, the wind speed at the outlet of the axial flow fans was unchanged at 10 m/s, and the rotating speeds of the ICVAWT were changed to 412, 494, 576, 659, and 741 rpm, respectively.

The power coefficients of the ICVAWT at the TSRs of 2.5, 3, 3.5, 4 and 4.5 were studied. The Reynolds number is  $7.8 \times 10^5$ .

The numerical simulation of the ICVAWT with two blades and the inverted cone angle of  $45^\circ$  was carried out using the CFD model established. The ICVAWT's size and inflow conditions of the simulation are the same as those of the wind tunnel experiment exactly.

Figure 10 shows that the trend of the power coefficient of the CFD results changing with the tip speed ratio is consistent with the experimental results. In the low TSR part, the difference between their power coefficients is very small, while in the high TSR part, the difference between the two becomes larger.

The reasons for the difference between the CFD results and the experimental results may be: (1) In the simulation analysis, the ICVAWT structure is simplified, only the blades are retained, the hub is removed, so the aerodynamic performance is better; (2) The power of the simulation is the actual shaft power of the wind turbine, while the experimental power is measured through the speed and torque

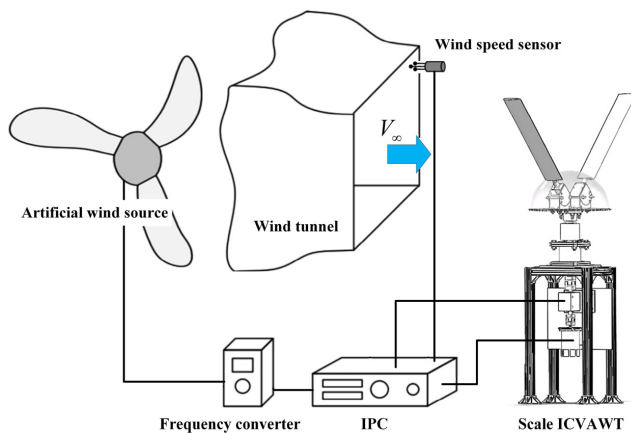


FIG. 9. Wind tunnel experiment platform.

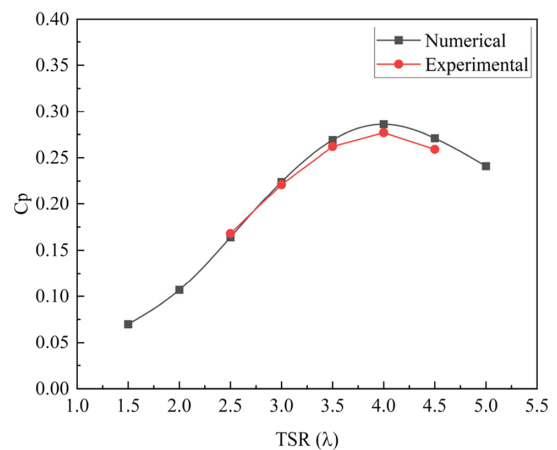


FIG. 10. Comparison between the numerical result and the experiment result.



TABLE IV. Labels of nine rotor configurations.

Number of blades (N)	Inverted cone angle ( $\gamma$ )		
	30°	45°	60°
2	2-30	2-45	2-60
3	3-30	3-45	3-60
4	4-30	4-45	4-60

sensor. Due to the presence of losses, the experimental results are inevitably lower than the simulation results.

The curve of the power coefficient obtained by the CFD model accurately evaluates the experimental results. we consider it sufficiently satisfactory to validate the CFD model and the CFD model validated is suitable to study and analyze the aerodynamic performance of ICVAWT with different rotor configurations.

#### IV. RESULTS AND DISCUSSION

The effects of the inverted cone angle and the number of blades on the aerodynamic performance of ICVAWT have been studied by the CFD method, and the optimal configuration of the ICVAWT rotor has been selected. 30°, 45° and 60° were selected for the inverted cone angle and 2, 3 and 4 were selected for the number of blades, so there are nine types of rotor configurations, as shown in Table IV. For each type of rotor configuration, the aerodynamic performance of the

ICVAWT was obtained by changing rotating speed of the ICVAWT. The reasons for these changes have been analyzed through the distribution and change of various physical quantities in the flow field.

#### A. Effect of inverted cone angle on the aerodynamic performance of the ICVAWT

To obtain the effect of the inverted cone angle on the aerodynamic performance of ICVAWT, we ensured that the number of blades remained unchanged and changed the inverted cone angle from 30° to 45° and 60°, and obtained the variation of the power coefficient with the TSR. ICVAWTs with different inverted cone angles have different maximum radius. Therefore, in order to ensure that ICVAWTs with different inverted cone angles have the same TSR, it is required to calculate the angular speed of ICVAWTs separately. For example, when the TSR is 3.5, the ICVAWTs with inverted cone of 30°, 45° and 60° needs to rotate at 0.389, 0.304, and 0.261 rad/s separately.

It can be concluded from Fig. 11 that with the increase in the TSR, the power coefficient first increases and then decreases. The TSR corresponding to the maximum power coefficient is called the optimal TSR. For the two blade configurations [Fig. 11(a)], the maximum power coefficients are 0.293 (TSR = 3.5) and 0.285 (TSR = 4) when the inverted cone angle are 30° and 45°, respectively. The maximum power coefficient is 0.206 (TSR = 4) when the inverted cone angle is 60°. For the three blades configurations [Fig. 11(b)], the maximum power coefficient is 0.309 (TSR = 3.5) when the inverted cone angle is

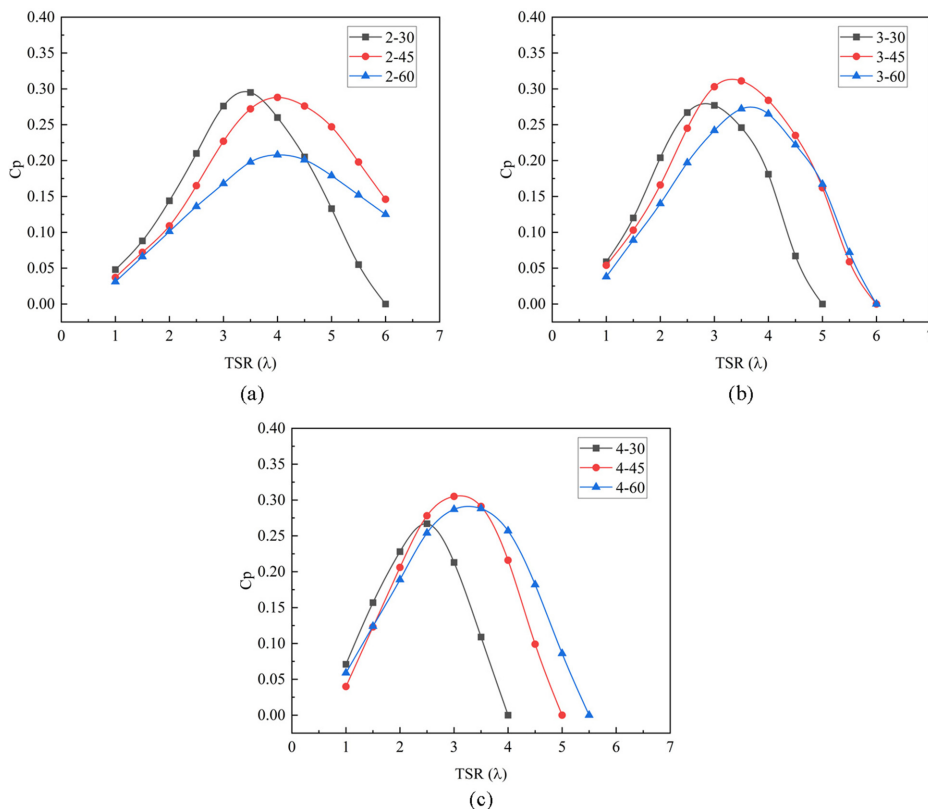


FIG. 11. Variation of power coefficient with TSR at the different inverted cone angles (a) Two blades (b) Three blades (c) Four blades.

Downloaded from http://pubs.aip.org/aip/rse/article-pdf/doi/10.1063/5.0145195/17795707/033305\_1\_5.0145195.pdf

45°, and 0.275 (TSR = 3) and 0.271 (TSR = 3.5) when the inverted cone angle is 30° and 60°, respectively. For the four blades configurations [Fig. 11(c)], the maximum power coefficients are 0.302 (TSR = 3) and 0.285 (TSR = 3) when the inverted cone angle is 45° and 60°, respectively, and the maximum power coefficient is 0.267 (TSR = 2.5) when the inverted cone angle is 30°. Therefore, for different blade numbers, when the inverted cone angle is 45°, the maximum power coefficients are all larger. The optimal TSRs at the inverted cone angle of 45° and 60° are larger than that at 30°, which indicates that the higher the inverted cone angle is, the faster the rotor speed is.

The effect of the inverted cone angle on the running stability of the ICVAWT with three blades was studied. Figure 12 shows the variation of the torque coefficient of a single blade and the whole rotor with the azimuthal angle when TSR is 3.5.

Figure 12(a) shows that with the increase in the inverted cone angle, the maximum  $C_M$  of a single blade in the upwind area decreases, while the maximum  $C_M$  in the downwind area increases and the load fluctuation amplitude of the blade decreases.

Figure 12(b) shows that with the increase in the inverted cone angle, the instantaneous  $C_M$  fluctuation amplitude of the wind turbine decreases significantly. The instantaneous  $C_M$  fluctuation amplitude of the ICVAWT configuration 3–30 is 0.106, the instantaneous  $C_M$  fluctuation amplitude of the ICVAWT configuration 3–45 is 0.0663, and the instantaneous  $C_M$  fluctuation amplitude of the ICVAWT configuration 3–60 is 0.0304. If the inverted cone angle of the rotor configuration is increased from 30° to 45° and 60°, the  $C_M$  of the ICVAWT decreases by 37.5% and 71.3%, respectively. The same rule also applies to other VAWT configurations with a different blade number.

### B. Effect of number of blades on the aerodynamic performance of the ICVAWT

To obtain the effect of the number of blades on the aerodynamic performance of ICVAWT, we ensured that the inverted cone angle remained unchanged and changed the number of blades from 2 to 3 and 4, and obtained the variation of the power coefficient with the TSR.

It can be concluded from Fig. 13 that with the increase in the number of blades, the optimal TSR decreases, indicating that the rated speed of the ICVAWT decreases, and the power coefficient decays faster at the high TSR, indicating that the stall phenomenon of a multi-blade ICVAWT is more obvious at high speed. For the rotor configurations with an inverted cone angle of 30° [Fig. 13(a)], the maximum power coefficient is 0.293 (TSR = 3.5) and 0.275 (TSR = 3) when the blade numbers are two and three, respectively. The maximum power coefficient is 0.267 (TSR = 2.5) when the blade number is four. For the rotor configurations with an inverted cone angle of 45° [Fig. 13(b)], the maximum power coefficients are 0.309 (TSR = 3.5) and 0.302 (TSR = 3) when the blade numbers are three and four, respectively. The maximum power coefficients are 0.288 (TSR = 4) when the blade number is two. For the rotor configurations with an inverted cone angle of 60° [Fig. 13(c)], the maximum power coefficients are 0.271 (TSR = 3.5) and 0.285 (TSR = 3) when the blade numbers are three and four, respectively. The maximum power coefficients are 0.206 (TSR = 4) when the number of blades is two. Therefore, for different inverted cone angles, when the blade number is three, the maximum power coefficients are all larger.

The effect of the number of blades on the running stability of the ICVAWT with the inverted angle of 45° was studied. Figure 14 shows the variation of the torque coefficient of a single blade and the whole rotor with the azimuthal angle when TSR is 3.5.

Figure 14(a) shows that with the increase in the number of blades, the  $C_M$  of a single blade in the upwind area decreases, but to a small extent. The  $C_M$  in the downwind area increases, but to a small extent too. Figure 14(b) shows that, with the increase in the number of blades, the instantaneous  $C_M$  fluctuation amplitude of the wind turbine decreases significantly and is closer to a straight line. The instantaneous  $C_M$  fluctuation amplitude of the rotor configuration with two blades is 0.207, that of the rotor configuration with three blades is 0.0671, and that of the rotor configuration with four blades is 0.0294. That is, if the blade number is increased from two to three and four, the  $C_M$  fluctuation amplitude of the ICVAWT decreases by 67.6% and 85.8%, respectively. The same rule applies to other rotor configurations with different inverted cone angles. Therefore, appropriately

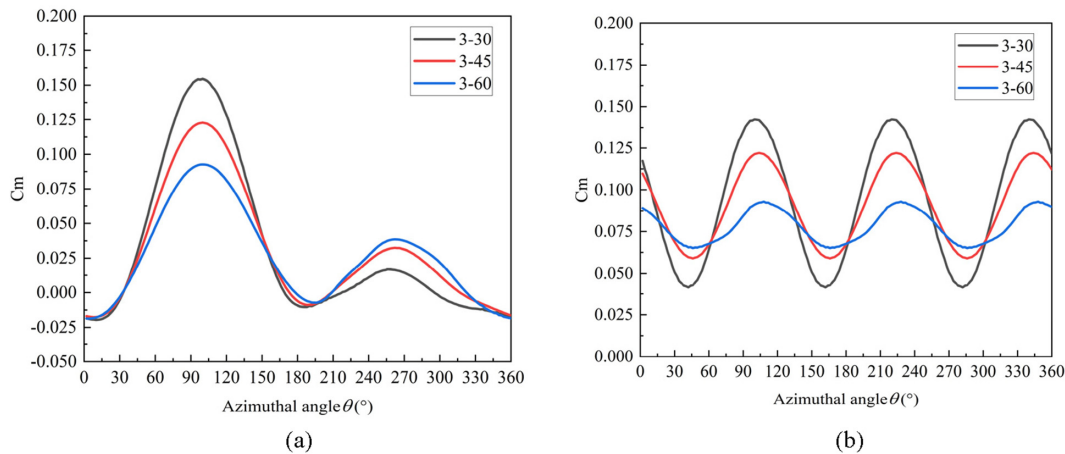


FIG. 12. Single blade and whole rotor torque coefficient for different inverted cone angles at TSR 3.5 (a) Single blade (b) Whole rotor.

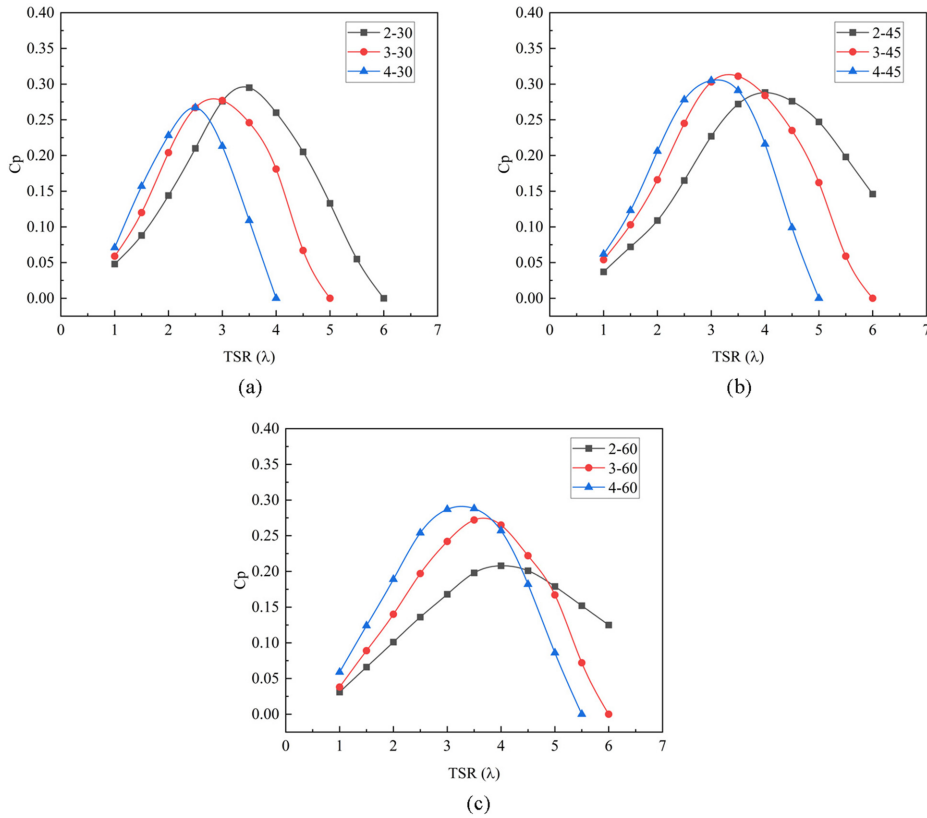


FIG. 13. Variation of power coefficient with TSR with the different number of blades (a) Inverted cone angle  $30^\circ$  (b) Inverted cone angle  $45^\circ$  (c) Inverted cone angle  $60^\circ$ .

increasing the blade number of the ICVAWT can greatly reduce the fluctuation of torque and output power during the operation.

### C. Flow field distribution and analysis of nine ICVAWT configurations

The flow field distribution of nine different wind turbine configurations is shown in Figs. 15, 16 and 17, which are, respectively, the

velocity contours, pressure contours and turbulence intensity contours at the middle height of the rotor when the ICVAWT is at the azimuthal angle of  $90^\circ$  and the TSR is 3.5. The ICVAWT rotation direction is counterclockwise.

Figure 15 shows that with the decrease in the inverted cone angle and the increase in the blade number, the induction factor of the incoming velocity of the blades becomes larger, and the velocity magnitude in the downwind area and behind the rotor decreases. With the

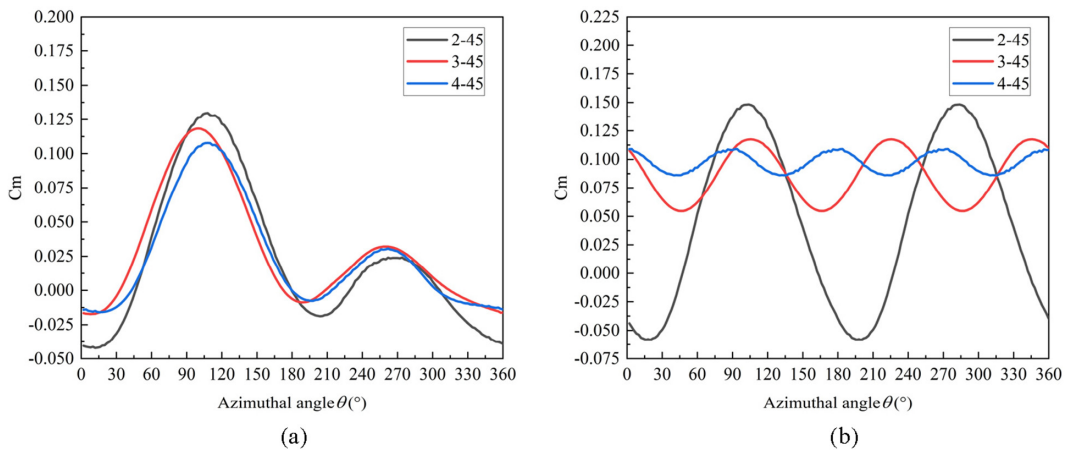


FIG. 14. Single blade and whole rotor torque coefficient for different blade numbers at TSR 3.5 (a) Single blade (b) whole rotor.

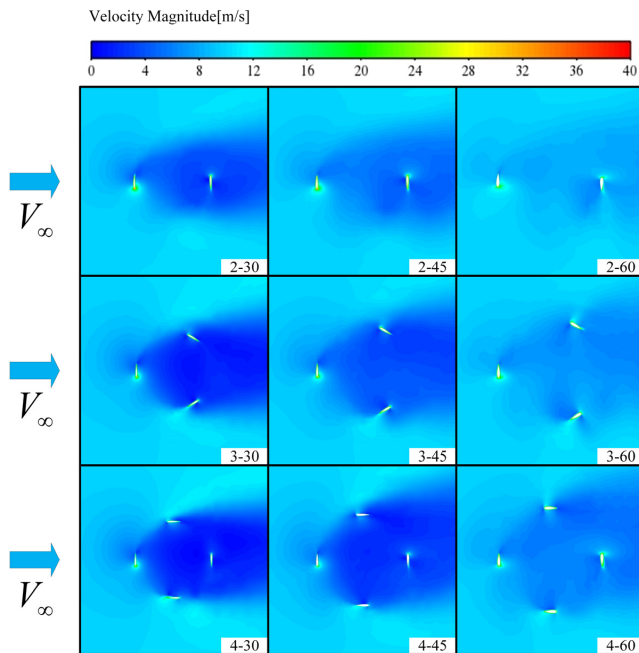


FIG. 15. Velocity magnitude contours for nine different rotor configurations.

increase in the inverted cone angle and the number of blades, the flow fields in the upwind and downwind areas are more similar, so the running stabilities under different rotor configurations are explained.

Figure 16 shows that with the increase in the inverted cone angle of the ICVAWT, the high-pressure area on the blades moves to the

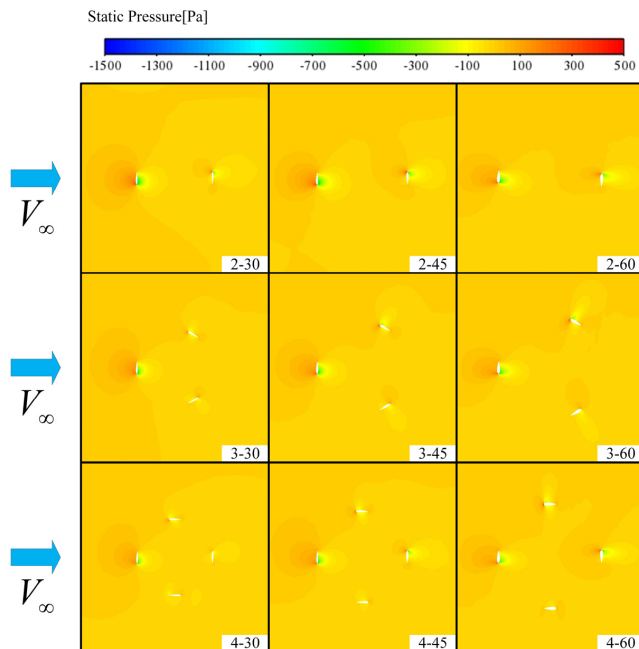


FIG. 16. Static pressure contours for nine different rotor configurations.

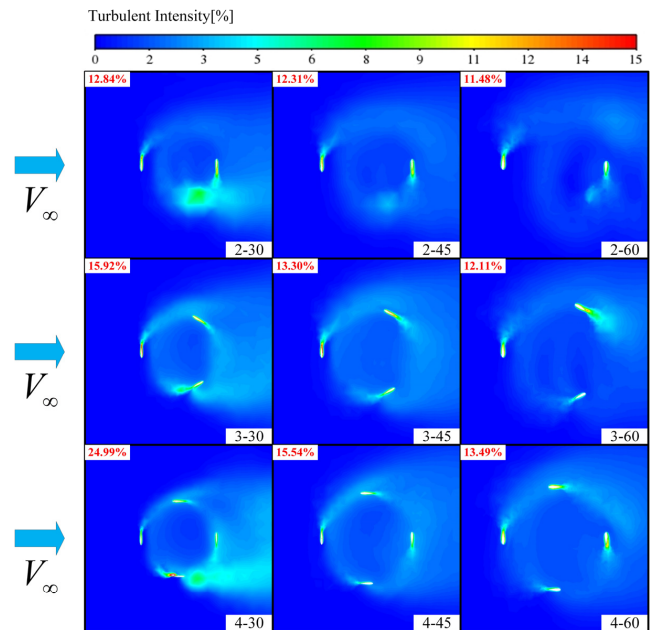


FIG. 17. Turbulent Intensity contours for nine different rotor configurations.

behind edge, and the included angle between the aerodynamic force generated by the pressure difference and the radial direction becomes smaller, leading to the reduction of the moment on the blade. With the increase in the blade number, the pressure difference on the blades decreases, and the torque of a single blade decreases.

Figure 17 shows the instantaneous turbulence intensity of different ICVAWT configurations at a typical position. Meanwhile, the averaged turbulence intensity data for one cycle is obtained for each ICVAWT configuration.

The turbulence intensity is calculated from one cycle mean data by dividing the variance of the wind velocity through the mean wind velocity<sup>28</sup>

$$t_{BT} = \frac{\sigma_u}{u}. \quad (19)$$

Figure 17 shows that with the increase in the inverted cone angle of the ICVAWT, the turbulence intensity of the flow field inside the wind turbine decreases. With the increase in the number of blades, the turbulence intensity of the flow field inside the ICVAWT increases, and the turbulence intensity around the blades increases, so the torque on a single blade decrease.

#### D. Aerodynamic performance analysis of the optimized ICVAWT rotor configuration

Considering power coefficient, running stability, the manufacturing cost of wind turbine and other factors, the inverted cone angle of 45° and three blades were selected as the optimized configuration of ICVAWT and the aerodynamic performance of the optimized configuration was studied.

Since ICVAWT is installed at a low place close to the sea plane, the offshore wind shear effect and the variation of turbulence intensity with height are considered.



TABLE V. Turbulence intensities at different heights.

Height (m)	Turbulence intensity
0–20	0.11
20–60	0.09
60–90	0.08
>=90	0.07

Considering the offshore wind shear effect, the inflow velocity is given by

$$V(y) = V_{BT} \left( \frac{z}{z_{BT}} \right)^\alpha, \tag{20}$$

where  $V_{BT}$  represents the velocity at the top of the wind turbine and  $V_{BT} = 10 \text{ m/s}$ ,  $z_{BT}$  represents the height of the top of the wind turbine and  $\alpha$  represents the offshore wind shear coefficient and  $\alpha = 0.08$ .

The variation of turbulence intensity with height is shown in Table V.

The aerodynamic performance of the optimized ICVAWT was studied using the above inflow velocity and turbulence intensity.

The CFD results and the experiment results are compared. The power coefficient curve and output power are shown in Fig. 18.

Figure 18(a) shows that the trend of the experimental results is consistent with the CFD results. In the low TSR part, there is little difference between the two. In the high TSR part, the difference between the two becomes larger. The optimal TSR is 3.5, the corresponding maximum  $C_p$  simulation result is 0.307, the experimental result is 0.295, and the error is 3.91%. Figure 18(b) shows that when the TSR is 3.5 and the inflow speed is 10 m/s, the numerical simulation result of output power is 2110.6 kW, and the experimental result converted by the power coefficient of the experiment is 2028 kW, with an error of 3.91%.

The variation of the torque coefficient with the azimuthal angle of a single blade and the ICVAWT at different TSRs was studied to discuss the stress of the ICVAWT in a cycle.

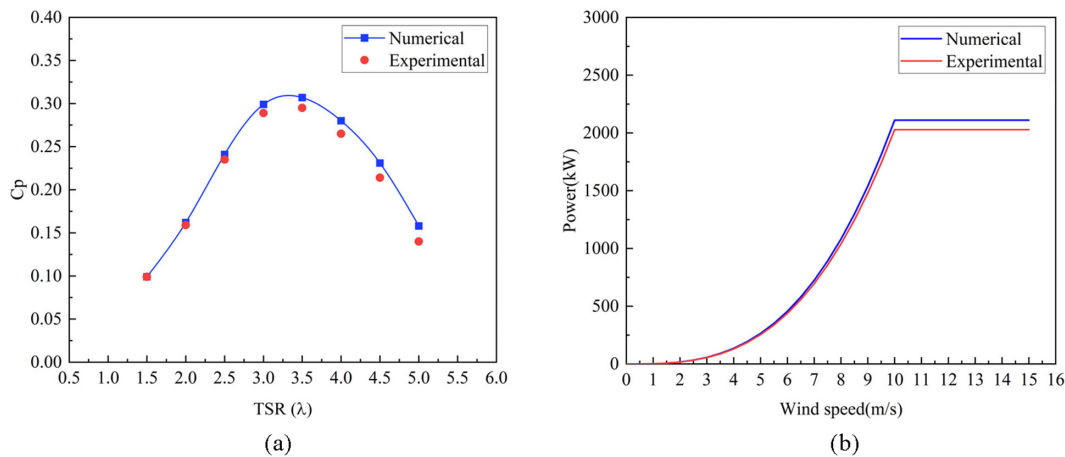


FIG. 18. Comparisons between CFD simulation results and experimental results (a) Power coefficient (b) Power output result.

Figure 19(a) shows that, with the increase in the TSR, the  $C_M$  of a single blade in the upwind area decreases and the  $C_M$  of a single blade in the downwind area is maximum when the TSR is optimal. The azimuthal angle related to the maximum  $C_M$  is maximum when the TSR is optimal. At that time ( $\lambda = 3.5$ ), the maximum  $C_M$  in the upwind area is 0.117 ( $\theta = 100^\circ$ ), and the maximum  $C_M$  in the downwind area is 0.03 ( $\theta = 258^\circ$ ). Figure 19(b) shows that with the increase in the TSR, the torque curve moves downward, and the  $C_M$  decreases more at the high TSR, that is, the average  $C_M$  decreases significantly. This is because the stall phenomenon intensifies at the high TSR, and the  $C_M$  of the ICVAWT decreases. From the variation of torque fluctuation amplitude, when the ICVAWT is at the optimal TSR, the torque fluctuation amplitude is the smallest, that is, the stability of the ICVAWT is the best when it is operating at the optimal TSR.

Figure 20 shows the pressure contours of the ICVAWT at different azimuthal angles and when the azimuthal angle is  $100^\circ$ , the force on the blade is maximum. From the pressure contours of the blades, it can be seen that the pressure difference mainly occurs at the trailing edge of the blades. The closer it is to the tip of the blades, the greater the pressure difference, indicating that the force generated by the blades is mainly at the higher position of ICVAWT.

The starting performance is a very important performance of VAWTs. For the three-blade wind turbine with an inverted cone angle of  $45^\circ$  and a wind velocity of 5 m/s, the torque coefficient that the wind turbine is subjected to when it is at different azimuthal angles is shown in Fig. 21. The starting performance of the ICVAWT was studied.

Figure 21 shows that when the ICVAWT is located at different azimuth angles, the starting torque varies greatly. For a three-blade wind turbine with an inverted cone angle of  $45^\circ$ , the starting torque coefficient is the maximum with a torque coefficient of 0.0333 when the rotor is at the azimuthal angle of  $110^\circ$ . When the ICVAWT is located at an azimuthal angle of  $60^\circ$ – $70^\circ$ , the starting torque coefficient is the maximum, with a torque coefficient of 0.0302. When the ICVAWT is located at an azimuthal angle of  $20^\circ$ – $40^\circ$ , the starting torque coefficient is the minimum, 0.0137–0.0153.

Figure 22 shows the velocity contour diagram and velocity streamline diagram of the ICVAWT when the azimuthal angle is  $90^\circ$ .

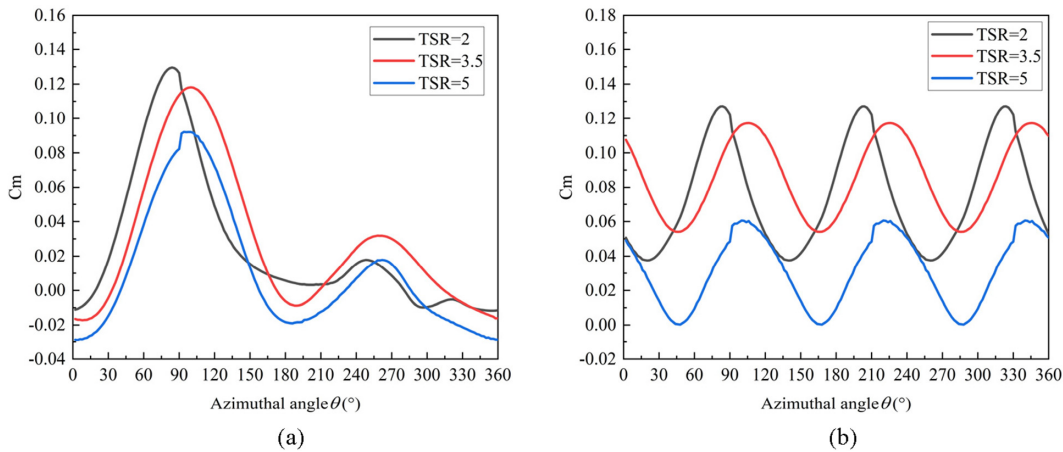


FIG. 19. Torque coefficient for three tip speed ratios  $\lambda_1 = 2, \lambda_2 = 3.5, \lambda_3 = 5$  (a) Single blade (b) Whole rotor.

The velocity magnitude changes mainly occur at the trailing edge and tip in the blade length direction, generating rotating torque. The flow field complexity of the VAWT can be seen from the 3D diagram, which also shows that the CFD simulation method can well capture

the detailed characteristics of the flow field, and has great value for academic research and engineering applications.

### V. CONCLUSION

A CFD model of 2 MW ICVAWT is established. The scale experimental prototype was designed based on the similarity theory and the wind tunnel experiment was carried out. The power coefficients obtained are consistent with the CFD results, and the error is small. The validity of the CFD model was verified. This CFD model has an important reference value for ICVAWT design and aerodynamic performance research.

For a different number of blades, the maximum power coefficient is higher when the inverted cone angle is  $45^\circ$ . For different inverted cone angles, the maximum power coefficient is higher when the blade number is three. When the inverted cone angle is  $45^\circ$  and the blade number is three, the ICVAWT has the highest power coefficient of 0.309, and the corresponding optimal TSR is 3.5. With the increase in the inverted cone angle and the number of blades, the instantaneous

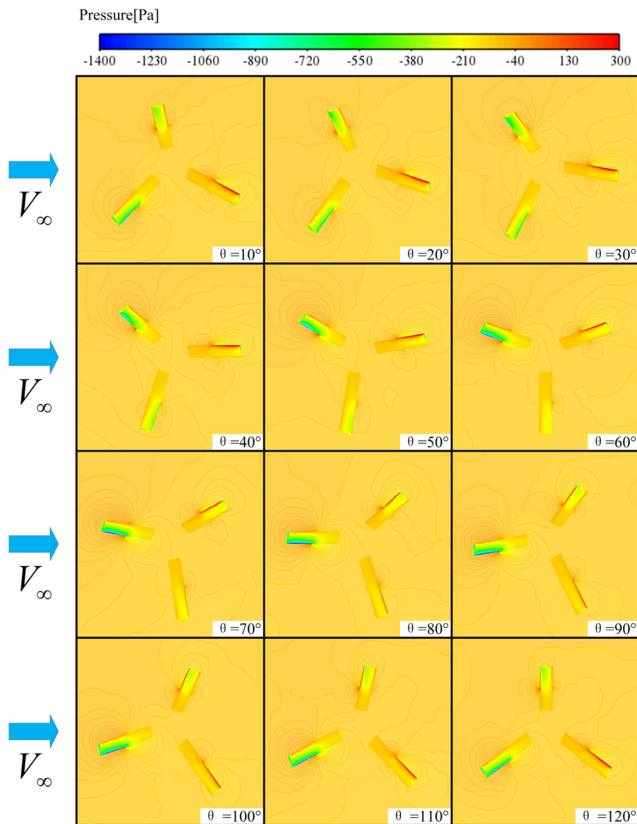


FIG. 20. Pressure contours for azimuthal angles of the rotor.

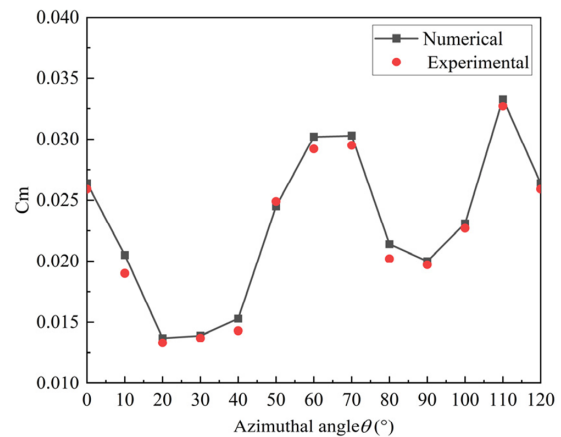


FIG. 21. Starting torque coefficient for the azimuthal angle at 5 m/s.

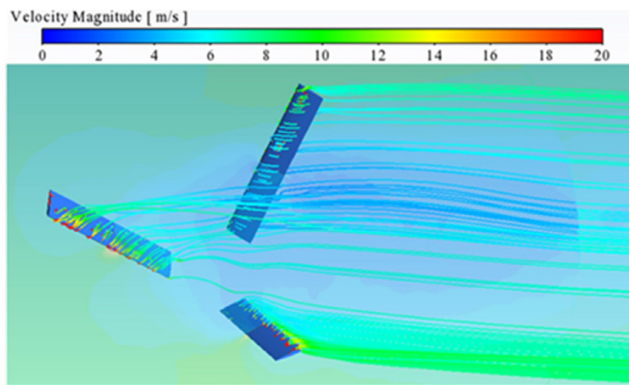


FIG. 22. ICVAWT 3D: velocity contours and streamlines at an azimuthal position  $\theta = 90^\circ$ .

torque coefficient fluctuation amplitude of the ICVAWT decreases significantly.

The power coefficient curve of the ICVAWT configuration with the highest power coefficient (inverted cone angle of  $45^\circ$ , three blades) is consistent with the changing trend of the experimental result. The difference between the two is very small in the low TSR part. As the TSR increases, the difference between the two becomes larger, and the error at the optimal TSR is 3.91%. The stability of the ICVAWT is the best at the optimal TSR. When the ICVAWT is at the azimuthal angle of  $110^\circ$ , the starting torque is the maximum, and its torque coefficient is 0.0333.

Further studies should investigate the airfoils, chord optimization and variable pitch to further improve the aerodynamic performance of the inverted cone vertical axis wind turbine.

## ACKNOWLEDGMENTS

This work was supported by the China Scholarship Council (Grant No. 202106120132).

## AUTHOR DECLARATIONS

### Conflict of Interest

The authors have no conflicts to disclose.

## Author Contributions

**Lei Zhang:** Conceptualization (equal); Methodology (equal); Software (lead); Validation (lead); Writing – original draft (lead). **Ao Wang:** Software (lead); Validation (supporting). **Jianjun Qu:** Supervision (equal); Writing – review & editing (lead). **Ernesto Benini:** Supervision (equal).

## DATA AVAILABILITY

The data that support the findings of this study are available from the corresponding author upon reasonable request.

## REFERENCES

<sup>1</sup>See <https://www.un.org/en/climatechange/paris-agreement> for the Paris Agreement.

- <sup>2</sup>J. R. Baker, “Features to aid or enable self starting of fixed pitch low solidity vertical axis wind turbines,” *J. Wind Eng. Ind. Aerodyn.* **15**(1–3), 369–380 (2003).
- <sup>3</sup>M. M. Aslam Bhutta, N. Hayat, A. U. Farooq, Z. Ali, S. R. Jamil, and Z. Hussain, “Vertical axis wind turbine—A review of various configurations and design techniques,” *Renewable Sustainable Energy Rev.* **16**(4), 1926–1939 (2012).
- <sup>4</sup>J. M. Jonkman and D. Matha, “Dynamics of offshore floating wind turbines—analysis of three concepts,” *Wind Energy* **14**(4), 557–569 (2011).
- <sup>5</sup>GWEC, see <https://www.gwec.net> for “Global Wind Report, 2022.”
- <sup>6</sup>T. Chaichana and S. Chaitep, “Wind power potential and characteristic analysis of Chiang Mai, Thailand,” *J. Mech. Sci. Technol.* **24**(7), 1475–1479 (2010).
- <sup>7</sup>I. Paraschivoiu, *Wind Turbine Design: Emphasis on the Darrieus Concept*, 1st ed. (Polytechnic International Press, Montreal, 2002).
- <sup>8</sup>P. Jamieson, *Innovation in Wind Turbine Design*, 1st ed. (Wiley, London, 2011).
- <sup>9</sup>M. R. Islam, S. Mekhilef, and R. Saidur, “Progress and recent trends of wind energy technology,” *Renewable Sustainable Energy Rev.* **21**, 456–468 (2013).
- <sup>10</sup>U. S. Paulsen, L. Vita, H. A. Madsen, J. Hattel, E. Ritchie, and K. M. Leban, “1st DeepWind 5 MW baseline design,” *Energy Proc.* **24**, 27–35 (2012).
- <sup>11</sup>L. Vita, U. S. Paulsen, H. A. Madsen, P. H. Nielsen, P. A. Berthelsen, and S. Carstensen, “Design and aero-elastic simulation of a 5 mw floating vertical axis wind turbine,” in *Proceedings of the ASME 31st International Conference on Ocean, Offshore and Arctic Engineering* (ASME, 2013), Vol. 7, pp. 383–392.
- <sup>12</sup>M. Cahay, E. Luquiau, C. Smadja, and F. Silvert, “Use of a vertical wind turbine in an offshore floating wind farm,” Paper presented at the Offshore Technology Conference, 2–5 May; Houston, TX (2011).
- <sup>13</sup>SKWID, *Floating Wind and Current Hybrid Power Generation* (Savonius Keel and Wind Turbine Darrieus, 2013).
- <sup>14</sup>T. Nakamura, K. Mizumukai, H. Akimoto, Y. Hara, and T. Kawamura, “Floating axis wind and water turbine for high utilization of sea surface area: Design of sub-megawatt prototype turbine,” in *Proceedings of the 32nd International Conference on Ocean, Offshore and Arctic Engineering* (ASME, 2013), p. 8.
- <sup>15</sup>AB S, see <https://seatwirl.com/> for SeaTwirl publish Year-end report.
- <sup>16</sup>J. Qu, Y. Zhao, and W. Yin, “A variable pitch high-power vertical axis wind power generation device and pneumatic start stop control method,” China Patent Bureau (Heilongjiang Province, 2019), No. CN105863957B.
- <sup>17</sup>G. Bedon, U. S. Paulsen, H. A. Madsen, F. Belloni, M. R. Castelli, and E. Benini, “Computational assessment of the DeepWind aerodynamic performance with different blade and airfoil configurations,” *Appl. Energy* **185**, 1100–1108 (2017).
- <sup>18</sup>T. J. Carrigan, B. H. Dennis, Z. X. Han, and B. P. Wang, “Aerodynamic shape optimization of a vertical-axis wind turbine using differential evolution,” *Int. Sch. Res. Notices* **2012**, 528418.
- <sup>19</sup>R. M. Bourguet, G. Harran, and M. Braza, “Aerodynamic multi-criteria shape optimization of VAWT blade profile by viscous approach,” in *Proceedings of the Euromech Colloquium 464b “Wind Energy”* (Springer, 2007), pp. 215–219.
- <sup>20</sup>E. J. Golloy and J. Honra, “Performance evaluation of a forward swept blade for vertical axis wind turbine through CFD simulation,” *IOP Conf. Ser.: Earth Environ. Sci.* **1**, 897 (2021).
- <sup>21</sup>K. M. Almohammadi, D. B. Ingham, L. Ma, and M. Pourkashan, “Computational fluid dynamics (CFD) mesh independency techniques for a straight blade vertical axis wind turbine,” *Energy* **58**, 483–493 (2013).
- <sup>22</sup>H. F. Lam and H. Peng, “Study of wake characteristics of a vertical axis wind turbine by two- and three-dimensional computational fluid dynamics simulations,” *Renewable Energy* **90**, 386–398 (2016).
- <sup>23</sup>Y. Wang, X. Sun, X. Dong, B. Zhu, D. Huang, and Z. Zheng, “Numerical investigation on aerodynamic performance of a novel vertical axis wind turbine with adaptive blades,” *Energy Convers. Manage.* **108**, 275–286 (2016).
- <sup>24</sup>L. Zhang and J. Qu, “Study on aerodynamic performance of a combined vertical axis wind turbine based on blade element momentum theorem,” *J. Renewable Sustainable Energy* **13**(3), 033304 (2021).

- <sup>25</sup>R. Amano and B. Sunden, *Aerodynamics of Wind Turbines: Emerging Topics* (WIT Press, 2014).
- <sup>26</sup>B. Hand, G. Kelly, and A. Cashman, "Numerical simulation of a vertical axis wind turbine airfoil experiencing dynamic stall at high Reynolds numbers," *Comput. Fluids* **149**, 12–30 (2017).
- <sup>27</sup>I. Bayati, M. Belloli, L. Bernini, H. Giberti, and A. Zasso, "Scale model technology for floating offshore wind turbines," *IET Renewable Power Gener.* **11**(9), 1120–1126 (2017).
- <sup>28</sup>M. Turk and S. Emeis, "The dependence of offshore turbulence intensity on wind speed," *J. Wind Eng. Ind. Aerodyn.* **98**(8–9), 466–471 (2010).